A&A 639, A99 (2020)
https://doi.org/10.1051/0004-6361/202038089

Astronomy & Astrophysics

Implications of different stellar spectra for the climate of tidally locked Earth-like exoplanets

Jake K. Eager[1], David J. Reichelt[1], Nathan J. Mayne[1], F. Hugo Lambert[2], Denis E. Sergeev[2], Robert J. Ridgway[1], James Manners[3,4], Ian A. Boutle[1,4], Timothy M. Lenton[3], and Krisztian Kohary[1]

[1] Physics and Astronomy, College of Engineering, Mathematics and Physical Sciences, University of Exeter, Exeter, EX4 4QL, UK
e-mail: j.k.eager@exeter.ac.uk
[2] Mathematics, College of Engineering, Mathematics and Physical Sciences, University of Exeter, Exeter, EX4 4QF, UK
[3] Global Systems Institute, University of Exeter, Exeter, EX4 4QE, UK
[4] Met Office, FitzRoy Road, Exeter, EX1 3PB, UK

Received 3 April 2020 / Accepted 23 May 2020

ABSTRACT

The majority of detected potentially habitable exoplanets orbit stars cooler than the Sun and are therefore irradiated by a stellar spectrum that peaks at longer wavelengths than the spectrum incident on Earth. Here, we present results from a set of simulations of tidally locked terrestrial planets orbiting three different host stars to isolate the effect of the stellar spectra on the simulated climate. Specifically, we perform simulations based on TRAPPIST-1e, adopting an Earth-like atmosphere and using the UK Met Office Unified Model in an idealised 'aqua-planet' configuration. Whilst holding the planetary parameters constant, including the total stellar flux (900 $\mathrm{W\,m^{-2}}$) and orbital period (6.10 Earth days), we compare results between simulations where the stellar spectrum is that of a quiescent TRAPPIST-1, Proxima Centauri, and the Sun. In simulations with cooler host stars, an increased proportion of incident stellar radiation was absorbed directly by the troposphere compared to the surface. This in turn led to an increase in the stability against convection, that is, a reduction in overall cloud coverage on the dayside (reducing scattering), leading to warmer surface temperatures. The increased direct heating of the troposphere also led to more efficient heat transport from the dayside to the nightside and therefore to a reduced day-night temperature contrast. We inferred that planets with an Earth-like atmosphere orbiting cooler stars had lower dayside cloud coverage, potentially allowing habitable conditions at increased orbital radii, compared to similar planets orbiting hotter stars for a given planetary rotation rate.

Key words. planets and satellites: atmospheres – planets and satellites: terrestrial planets

1. Introduction

Several potentially habitable terrestrial exoplanets have been detected, including Proxima Centauri b (Anglada-Escudé et al. 2016) and TRAPPIST-1e (Gillon et al. 2017), orbiting M dwarf stars, which are smaller and cooler than the Sun (G dwarf). The change in the host star brightness and temperature leads to two important consequences. Firstly, for a planet to orbit in the habitable zone (Kasting et al. 1993) around an M dwarf, it must have a smaller orbital radius (and therefore shorter period) than the orbital radius of Earth. Therefore the planet will experience stronger tidal forces from the host star than the Earth does from the Sun, which is likely to result in the planetary rotation rate and orbital period becoming synchronised; this is known as tidal locking (Pierrehumbert & Hammond 2019). Secondly, the amount of stellar radiation incident on the planet peaks at longer wavelengths because the temperature of M dwarfs is lower than that of G dwarfs (e.g. see Joshi & Haberle 2012; Shields et al. 2013; Rushby et al. 2019). Another important difference between G and M dwarfs is the occurrence rates and strength of stellar flares, and the overall stellar activity, which are both much higher in M dwarfs (e.g. see Howard et al. 2018, for Proxima Centauri). This has important implications for both the atmospheric composition, for example, in terms of stratospheric ozone cycling (Yates et al. 2020), and the habitability of planets orbiting such stars. Initial studies have been performed in 1D (Tilley et al. 2019), but extension to 3D is required given the assumption of tidal locking for planets such as TRAPPIST-1e and Proxima Centauri b, resulting in a permanent dayside and nightside, the latter receiving no direct stellar irradiation. In this work we focus on the differences caused exclusively by the quiescent stellar spectra and reserve inclusion of stellar activity for future work.

The climates of the TRAPPIST-1 planets (Wolf 2017; Turbet et al. 2018; Fauchez et al. 2020) and Proxima Centauri b (Turbet et al. 2016; Boutle et al. 2017, 2020; Del Genio et al. 2019) have been simulated using different model infrastructures and exploring different facets of the climate system. The vast majority of these simulations reveal a similar dynamical structure of a dominant, coherent, zonal flow or jet that transports heat from the dayside to nightside. However, a direct comparison to isolate the significance of the spectrum of the host star has yet to be performed. The effect of stellar type through differing atmospheric absorption on cloud, convection, and day-night heat and moisture transport are key in determining the impact that the differences in the spectra – between different host stars – will have on the planetary climate.

For terrestrial exoplanets, Yang et al. (2013) demonstrated that clouds produce a negative feedback that extends the inner edge of the habitable zone. As the overall stellar irradiance increases, so does convection, cloud coverage, and consequently, the albedo on the dayside, thus cooling the planet. This is only

possible if there is a large water supply on the dayside of the planet (e.g. on an aquaplanet). Yang & Abbot (2014) and Koll & Abbot (2016) employed two-box (dayside and nightside) models to determine what controls the surface temperature. Yang & Abbot (2014), in particular, showed that the nightside of the planet acts as a "radiator fin" , allowing outgoing longwave radiation (OLR) to escape from the atmosphere, which cools the planet because of the low level of high-altitude cloud. This is because on the dayside, the water vapour and cloud greenhouse effects reduce the efficiency of the local atmosphere in radiating stellar energy into space. This energy is instead transported by the atmosphere to the nightside, where there is a strong temperature inversion, and the cloud greenhouse effect is negligible, so that infrared energy is easily emitted into space. Yang & Abbot (2014) showed that when the emissivity of the nightside is increased, the dayside surface temperature decreases significantly, whereas increasing dayside emissivity leads to small increases in temperature.

Boutle et al. (2017) showed that for a simulation of Proxima Centauri b, vigorous convection over the sub-stellar point acted to transport heat and moisture vertically to the altitude of the zonal jet. Recently, Sergeev et al. (2020) have explored the differences obtained when employing various treatments and parametrisations of convection within 3D simulations of a tidally locked terrestrial exoplanet, and performing high-resolution convection-permitting simulations free from such approximated treatments. Sergeev et al. (2020) showed that important differences in the vertical and horizontal transport of heat and moisture exist between coarse-resolution, employing convection parametrisations, and high-resolution simulations with explicit convection. However, these studies have not yet been extended to explore the impact of differing stellar spectra on the behaviour of the convective transport, cloud coverage, and day-night transport.

The impact different stellar spectra have on a planetary climate has been studied for rapidly rotating planets (Shields et al. 2013). Shields et al. (2013) found that when holding the total stellar irradiance received by a planet constant, planets orbiting cooler, redder stars exhibit higher global mean surface temperatures than those orbiting warmer stars. This was due to increased direct absorption of incident stellar radiation by the atmosphere for planets orbiting cooler stars. The stellar spectrum of an M dwarf overlaps considerably more with the absorption features of CO_2 and H_2O than that of a G dwarf, with the former emitting a larger fraction of radiation in the near-infrared (Pierrehumbert 2010). Shields et al. (2013) also found that the H_2O ice albedo feedback (where, as ice forms, more light is reflected from the planetary surface, leading to further cooling and increased ice coverage) was weaker for planets orbiting cooler stars. This is due to the wavelength dependence of the ice albedo, which decreases with wavelength above 0.5 μm, leading to a lower contrast between ice and water (Joshi & Haberle 2012). Shields et al. (2019) took this further to find that a planet orbiting an M dwarf absorbs 12% more incident solar energy than its G dwarf counterpart for an Earth-like configuration with a 24-hour rotational period. Meanwhile, Yang et al. (2019a) found that an increase in atmospheric absorption of stellar radiation led to an increase in relative humidity at higher altitudes globally, causing a significant decrease in OLR.

In this study, we extend on previous works by investigating the effect that different stellar spectra have on the planetary climate of tidally locked planets with Earth-like atmospheres, focusing on cooler stars around which current, potentially habitable, targets have been detected. We performed simulations using the Met Office 3D climate model, the Unified Model (UM), based on the planetary parameters for TRAPPIST-1e, and a 1 bar N_2 dominated atmosphere with 400 ppm CO_2. Further simulations were performed, replacing the stellar spectrum of TRAPPIST-1 with that of Proxima Centauri and the Sun, holding all other parameters constant, and retaining a tidally locked configuration. Setting a constant rotation rate across our experiments would not be physically consistent with tidally locked planets obeying Kepler's laws. However, the effect of changes in the rotation rate on exoplanet climates has been well studied (e.g. Merlis & Schneider 2010; Haqq-Misra et al. 2018; Penn & Vallis 2018; Komacek & Abbot 2019) and is not our focus here. Additionally, increasing the gravity in a simulation of a given planet leads to a cooling for cases where a dilute, radiatively active condensible (such as water in our configuration) is present (Thomson & Vallis 2019; Yang & Yang 2019). Therefore, as we look to isolate the effect that changing the stellar spectrum has on the planetary climate, we maintain a constant top-of-atmosphere (TOA) incident flux, orbital period, atmospheric composition, and planetary mass and radius for all our simulations.

In Sect. 2 we give an overview of the UM (which has now been employed and detailed in many exoplanet studies) and our specific configurations, followed by presenting our results in Sect. 3. In Sect. 3.1 we explore the basic climatology of our simulations through the surface temperature and winds. This is followed by investigation of the moisture and cloud coverage in Sect. 3.2, and separation of the radiative, advective, latent, and boundary-layer turbulent contributions to the heating and evaporation or condensation in Sect. 3.3. Finally, in Sect. 4 we present our conclusions and discuss both the limitations of our approach and the potential implications for the habitability of tidally locked planets with Earth-like atmospheres. We find that planets orbiting cooler stars absorb more shortwave stellar radiation directly in the troposphere, which leads to more efficient zonal circulation and a smaller temperature gradient between the day- and nightside. The increase in the ratio of radiation absorbed by the atmosphere compared to the surface results in a dayside with less vigorous convection, which reduces dayside cloud cover and hence the overall planetary albedo. This results in planets orbiting cooler stars being globally warmer than those orbiting hotter stars. Overall, we find that planets orbiting cooler stars have larger regions on the dayside that can support liquid water, and we infer that such planets likely maintain habitable temperatures out to larger orbital radii (and lower overall incident stellar fluxes) than their counterparts orbiting hotter stars.

2. Model setup

In this work we use the Met Office general circulation model (GCM), the UM, which has been adapted to a range of exoplanet applications and used for a large number of studies covering hot Jupiters (Mayne et al. 2014a, 2017; Amundsen et al. 2016; Helling et al. 2016; Tremblin et al. 2017; Drummond et al. 2018a,b, 2020; Lines et al. 2018a,b, 2019; Sainsbury-Martinez et al. 2019; Debras et al. 2019, 2020), mini-Neptunes/Super Earths (Drummond et al. 2018c; Mayne et al. 2019) and terrestrial planets (Mayne et al. 2014b; Boutle et al. 2017, 2020; Lewis et al. 2018; Fauchez et al. 2020; Yates et al. 2020; Joshi et al. 2020; Sergeev et al. 2020). For this work, we follow a similar configuration to that of Boutle et al. (2017) and Lewis et al. (2018), based on the Global Atmosphere 7.0 configuration (Walters et al. 2019). The UM has implemented the ENDGame dynamical core, which uses a semi-implicit semi-Lagrangian formulation to solve the non-hydrostatic, fully compressible deep

Table 1. Stellar parameters for TRAPPIST-1 (Fauchez et al. 2020), Proxima Centauri (Schlaufman & Laughlin 2010), and the Sun as well as the semi-major axis for the planet in our simulations.

Host star	Effective temperature (K)	g (m s^{-2})	Metallicity (dex)	Semi-major axis (AU)
TRAPPIST-1	2600	1000	0	0.02928
Proxima Centauri	3000	1000	0.3	0.04800
The Sun	5700	274	0.012	1.230

atmosphere equations of motion (Wood et al. 2014). Processes that occur on a scale smaller than the size of the grid boxes are parametrised. Convection uses a mass-flux approach based on Gregory & Rowntree (1990), water clouds use the PC2 scheme detailed in Wilson et al. (2008), incorporating mixed-phase microphysics based on Wilson & Ballard (1999), and turbulent mixing uses an approach based on Lock et al. (2000) and Brown et al. (2008). The simulations were configured as an aquaplanet, using a single-layer slab-homogeneous flat surface as the inner boundary (planetary surface), which is based on Frierson et al. (2006). It represents an ocean surface with a 2.4 m mixed layer with a heat capacity of 10^7 J K^{-1} m^{-2}, with no horizontal heat transport. The emissivity of the surface is fixed at 0.985 and the albedo is spectrally dependent and varies with stellar zenith angle, based on Jin et al. (2011). Sea-ice formation is not considered in the model, with the surface remaining as liquid water throughout. The Suite of Community Radiative Transfer codes based on Edwards and Slingo (SOCRATES) scheme treats the radiative transfer in the UM, employing the correlated-k method. SOCRATES has been adapted and tested for a range of exoplanet configurations (e.g. Amundsen et al. 2014, 2017), but in this work, we use a configuration similar to that used to study Earth (Walters et al. 2019). Longwave "planetary" radiation is treated via 12 bands (between 3.3 and 10 mm), while shortwave "stellar" radiation is treated by 29 bands (0.20–20 μm) with the opacity data obtained from the NASA Goddard Institute for Space Studies[1].

As our focus is the effect that different host star emission has on the climate of a planet, we used input spectra for three different stars: TRAPPIST-1, Proxima Centauri, and the Sun. The stellar parameters for these stars are shown in Table 1, and their spectra are shown in Fig. 1 (top), generated using the BT-settl model of theoretical spectra (Rajpurohit et al. 2013). Figure 1 (middle) shows the wavelength dependence of the absorption cross section for water vapour (Polyansky et al. 2018) and carbon dioxide (Tashkun & Perevalov 2011). The absorption cross sections were generated using the ExoMol (Tennyson et al. 2016) database, and the ExoCross software (Yurchenko et al. 2018), for an atmospheric pressure and temperature of ~800 hPa and ~230 K, respectively. The solar emission peaks at visible wavelengths, whereas TRAPPIST-1 and Proxima Centauri peak in the infrared, with a larger fraction of the radiation emitted at >1 μm, which is the region where carbon dioxide and, in particular, water vapour begin to absorb. TRAPPIST-1 is the coolest star and emits more radiation at longer wavelengths than Proxima Centauri for a constant total flux. Figure 1 (bottom) shows the radiative properties of the cloud. Scattering for both an ice and a liquid-water cloud remains relatively constant across the stellar spectrum, and thus the cloud albedo will remain constant between the simulations for the same cloud distributions.

[1] From directories sp_sw_dsa_ar and sp_lw_dsa_ar at https://portal.nccs.nasa.gov/GISS_modelE/ROCKE-3D/spectral_files/

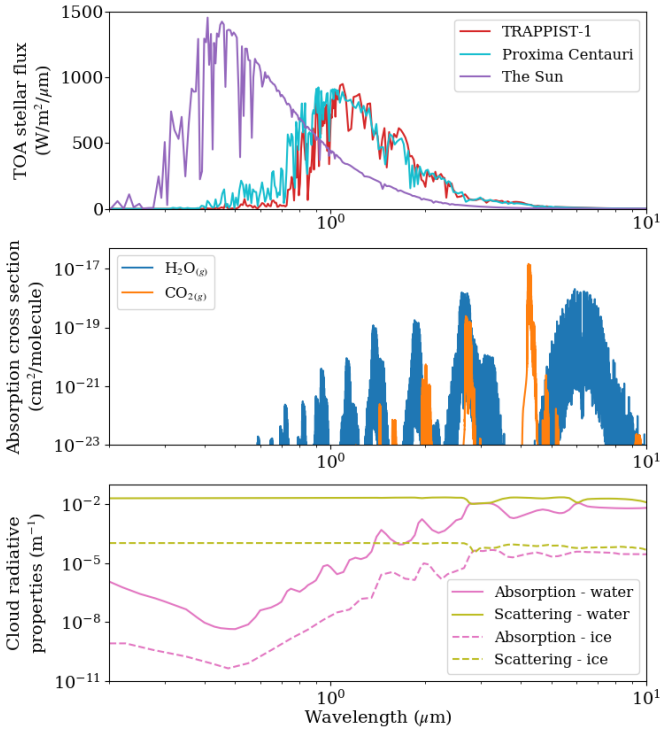

Fig. 1. Wavelength vs. stellar flux per wavelength (*top*), received at the TOA for a planet orbiting TRAPPIST-1 (red), Proxima Centauri (cyan), and the Sun (purple), with a fixed total stellar flux of 900 W m^{-2}. Stellar profiles were created using the BT-settl model grid of theoretical spectra (Rajpurohit et al. 2013) with stellar parameters from Table 1. *Middle panel*: absorption cross section per molecule for water vapour (blue) (Polyansky et al. 2018) and carbon dioxide gas (orange) (Tashkun & Perevalov 2011) against wavelength. Absorption cross sections (*centre*) are for a pressure of ~800 hPa and an air temperature of ~230 K using the ExoMol (Tennyson et al. 2016) database, generated using ExoCross (Yurchenko et al. 2018). Also shown are the cloud absorption (pink) and scattering (green) rates for liquid water (solid) and water ice (dashed). These assume typical cloud droplet radii of 9 μm and 30 μm for a liquid and an ice cloud, respectively.

In terms of absorption rates, both ice and liquid-water clouds have global minima at the peak of the solar spectrum at ~0.4 μm, while Proxima Centauri and TRAPPIST-1 peak where cloud absorption rates are about three orders of magnitude higher. We can thus expect that there will be increased atmospheric absorption by clouds for the cooler stars.

As discussed, in order to isolate the impact of the different stellar spectra, we performed three simulations, all with the planetary parameters of TRAPPIST-1e, taken from Gillon et al. (2017) and Grimm et al. (2018) and shown in Table 2. The parameters are consistent with those used recently by Fauchez et al. (2020). The simulations use the input stellar spectra for TRAPPIST-1, Proxima Centauri, and the Sun shown in Fig. 1; we call them T1:T1e, ProC:T1e, and Sun:T1e, respectively. As

Table 2. Parameters used for all planetary configurations, based on TRAPPIST-1e from Gillon et al. (2017), Grimm et al. (2018) and Fauchez et al. (2020).

Parameter	
Stellar irradiance ($W\,m^{-2}$)	900
Orbital period (Earth days)	6.10
Angular frequency ($rad\,s^{-1}$)	1.19×10^{-5}
Eccentricity	0
Obliquity (°)	0
Radius (km)	5800
Surface gravity ($m\,s^{-2}$)	9.12

our primary focus is investigating the effect of different stellar spectra of our three host stars, we maintained a fixed total stellar irradiance at the planet. In practice, this required altering the orbital semi-major axis, with the values show in Table 1. In reality, we would expect the orbital period to increase with semi-major axis according to Kepler's third law, with a commensurate change expected in the rotation rate to retain a tidally locked configuration. However, as changes in the rotation rate lead to well-studied changes in the circulation and climate (Merlis & Schneider 2010; Penn & Vallis 2018), we adopted a constant orbital period and angular frequency of rotation. The simulations were also performed at zero obliquity and eccentricity, consistent with tidal locking. It is important to note that simulations ProC:T1e and Sun:T1e were not designed to represent any particular planet, but solely to investigate the isolated impact of the different stellar spectra.

All simulations used a horizontal resolution of 2.5° in longitude by 2° in latitude, with 38 vertical levels between the surface (z = 0 km) and the TOA (z = 40 km). The vertical levels were quadratically stretched to enhance the resolution at the surface. All simulations ran for 8000 Earth days, with a time step of 1200 seconds, with equilibrium being reached after 1000 Earth days, as determined through stable global mean surface temperatures and balance of the TOA flux (not shown). The data presented in Sect. 3 are temporal averages from 1000 to 8000 days, and where a vertical coordinate was used, the data were converted from the model height grid into σ, where $\sigma = p/p_s$ and p is the pressure and p_s the surface pressure for that specific model column. The global average surface pressure for all simulations was 1 bar. The sub-stellar point, the point closest to the host star, was located at (0, 0)° and the anti-stellar point, the point farthest from the host star, was located at (0, 180)°. Finally, spatial averages are also presented in Sect. 3, where dayside-averaged quantities include data from −90° to 90° in latitude and −90° to 90° in longitude, and nightside-averaged quantities include data from −90° to 90° in latitude and −180° to −90° and 90° to 180° in longitude. Units given in terms of days refer to the duration of an Earth day. UM output was processed and plotted using the Python packages Iris (Met Office 2010-2020) and Matplotlib (Hunter 2007).

3. Results

In this section we present results from our three simulations T1:T1e, ProC:T1e, and Sun:T1e. This begins with the basic temperature and wind structure (Sect. 3.1), before we explore the moisture, cloud coverage, and the subsequent effect on the radiation budget (Sect. 3.2). We conclude with the components contributing to the heat and water vapour budget (Sect. 3.3).

3.1. Surface temperature and atmospheric dynamics

A natural metric to describe the basic climatic state is the surface temperature. Figure 2 shows the surface temperature variation across latitude and longitude for our three simulations, with the winds at 10 m shown as vector arrows. The left panel shows the absolute surface temperature for case T1:T1e, differences are then shown by subtracting the T1:T1e temperature field from either the ProC:T1e or Sun:T1e results as the middle and right panels, respectively. Figure 2 shows that as the temperature of the host star increases (left to right), the planetary surface temperature generally decreases. The greatest cooling is seen on the nightside, predominantly at the equator, with some warming in the polar regions of the ProC:T1e case. This suggests that there may be an asymmetry between the changes in the meridional and zonal transport efficiency. The region of the surface above 273 K is enclosed by the black contour in Fig. 2. These regions are similar in magnitude in cases T1:T1e and ProC:T1e, but case Sun:T1e does not have a substantial region of the planetary surface that may sustain liquid water, and it may be considered less habitable as a result. All simulations have similar near-surface winds, showing a convergence towards the sub-stellar point, because solar forcing gives rise to a region of intense convection, as discussed in Boutle et al. (2017) and Sergeev et al. (2020).

Table 3 shows the spatial average dayside, nightside, and global surface temperatures for the three simulations. The values in Table 3 confirm that the simulation with the coolest star, T1:T1e, is the warmest, and case Sun:T1e exhibits the coldest temperatures. The day-night temperature contrast is lowest for simulation T1:T1e, suggesting the most efficient day-night circulation of the three simulations, and case Sun:T1e has the highest contrast and weakest circulation. Cases T1:T1e and ProC:T1e have similar temperatures; T1:T1e is consistently warmer by about 1 K. The small differences in stellar spectra between TRAPPIST-1 and Proxima Centauri (Fig. 1) may have a small effect on planetary climate, which is only amplified by higher contrasts in effective stellar temperature.

The dominant component of the heat redistribution from the day- to nightside of the planet is the zonal jet (e.g. Lewis et al. 2018). Figure 3 shows the longitudinal (and temporally) averaged zonal wind for latitude against σ, shown for simulations T1:T1e (left), ProC:T1e (middle), and Sun:T1e (right). The super-rotating equatorial jet reduces in magnitude as the host star increases in temperature (left to right). As shown by Showman & Polvani (2010, 2011), the zonal jet is accelerated via large-scale wave patterns that are driven by the day-night temperature contrast, and it is further shaped by the vertical and latitudinal heating gradients. Lewis et al. (2018) also showed that changes in the radiative properties of the surface, that is, moving from bare land to ocean, resulted in a change in the temperature structure and thereby in a change in the jet acceleration. Our simulations show an increase in the overall absorption of radiation on the dayside from hotter to cooler stars (see Sect. 3.2). This might be expected to result in a higher day-night temperature contrast for cooler stars, as opposed to the reduction shown in Table 3. However, as the absorption is dominated by the atmosphere (as opposed to the surface), this results in a day-night contrast that extends over a wider range of pressures, that is, higher into the atmosphere for cooler stars (see Sect. 3.2). We speculate that this acts to extend the vertical region over which momentum convergence acts to accelerate the jet, and indeed, the jet structure persists over a broader vertical (and meridional) range for the simulations of cooler stars, as shown in Fig. 3. The vertical

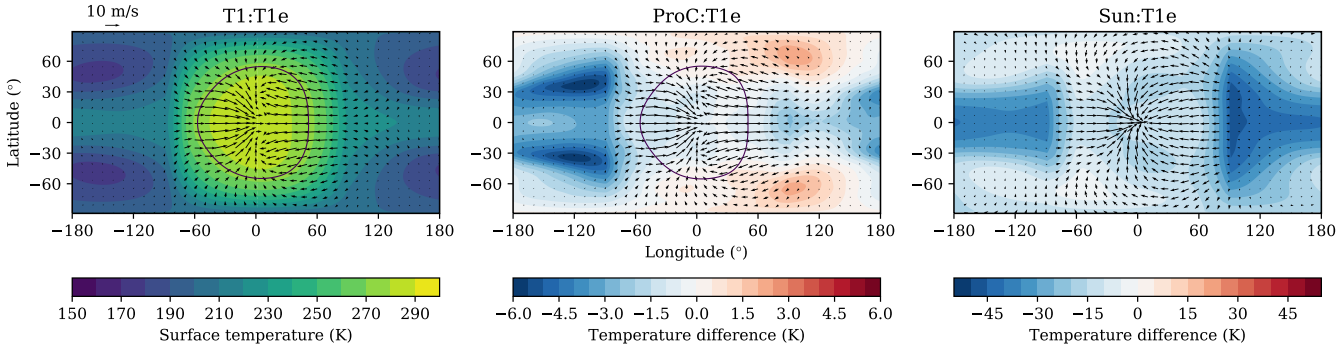

Fig. 2. Map of the surface temperatures (colour scale) for the T1:T1e simulation (*left*). The following two plots show the difference in surface temperature from T1:T1e for cases ProC:T1e (*middle*) and Sun:T1e (*right*). A negative difference (blue) indicates a cooler surface than T1:T1e. Near-surface (10 m) wind vectors (arrows) are also shown in each plot. The sub-stellar point is located at (0°, 0°). A contour (black) is shown for the 273 K surface isotherm, but this temperature is not reached over an extended region for case Sun:T1e. The colour scale for ProC:T1e and Sun:T1e is different. Only the temperature field is subtracted, the winds are the unaltered values for each simulation.

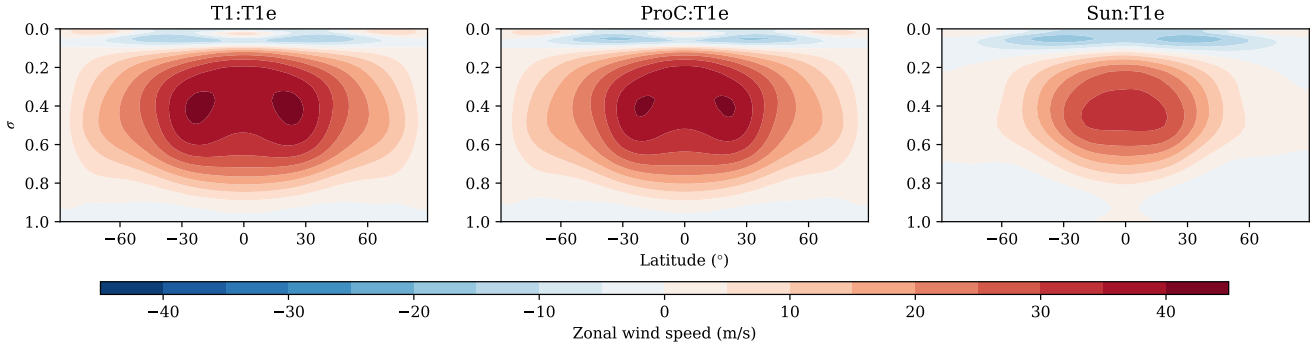

Fig. 3. Latitude vs. σ (pressure divided by surface pressure), showing the zonal wind speed (colour scale), taken as a longitudinal average for simulations T1:T1e (*left*), ProC:T1e (*middle*), and Sun:T1e (*right*). Positive values for the zonal wind (red) represent eastward flow.

Table 3. Mean surface temperatures for global, dayside, and nightside, and the temperature contrast (nightside subtracted from dayside) for T1:T1e, ProC:T1e, and Sun:T1e.

Simulation	Temperature (K)			
	Global	Dayside	Nightside	Contrast
T1:T1e	231.2	260.8	201.6	59.2
ProC:T1e	229.8	260.1	199.5	60.6
Sun:T1e	209.4	245.5	173.4	72.1

component of momentum convergence has been shown to be vital for accelerating super-rotating equatorial flows (Showman & Polvani 2011) in hot Jupiters, and we have studied the detailed wave responses in these cases (Debras et al. 2019, 2020). However, we reserve such a detailed study of these simulations for future work, and simply note here that the jet is stronger for planets orbiting cooler stars, and the flow acts to transport heat and, critically, moisture zonally around the planet. Planets orbiting cooler stars can also have a stronger nightside equatorial return flow near the surface, as shown in Fig. 2.

3.2. Moisture and cloud in the atmosphere

Water vapour and cloud play an important role in the radiation budget, particularly in shaping the OLR and in determining the contributions of the atmosphere compared to the planetary surface. Figure 4 shows the OLR for our three simulations after subtraction of the longwave surface emission.

All the simulations show the same pattern of dayside OLR originating from colder levels in the atmosphere than the surface, which is due to high-altitude clouds and water vapour. The nightside OLR indicates emission from warmer levels than the surface because of cloud and water vapour around the nightside temperature inversion and the lack of high-altitude cloud. In the rest of this section we investigate the changes in moisture and cloud coverage and use this to understand the changes in radiation emission between the simulations.

Moisture transport from the dayside to the nightside of a tidally locked planet is important because of its effect on the OLR, both directly or through subsequent cloud formation (Yang & Abbot 2014). Generally, moisture is transported upward from the surface through convection in the sub-stellar region. This also leads to cloud formation, with the zonal jet transporting moisture (and cloud) horizontally high up in the troposphere. Subsidence and further condensation occur on the nightside (Yang & Abbot 2014; Boutle et al. 2017; Lewis et al. 2018; Sergeev et al. 2020). To explore this for our simulations, Fig. 5 shows the column-integrated water content as a function of latitude and longitude. The left panel shows the absolute water-vapour column content for simulation T1:T1e, while the middle and right panels show the percentage change in water-vapour column content for simulations ProC:T1e and Sun:T1e after subtraction of an equivalent T1:T1e water-vapour content. However, as the dominant factor in the moisture content variation is due to the temperature change through the Clausius-Clapeyron relation, we attempted to remove this component. To do this, we calculated the difference in relative humidity of cases ProC:T1e and Sun:T1e from the T1:T1e case and integrated the

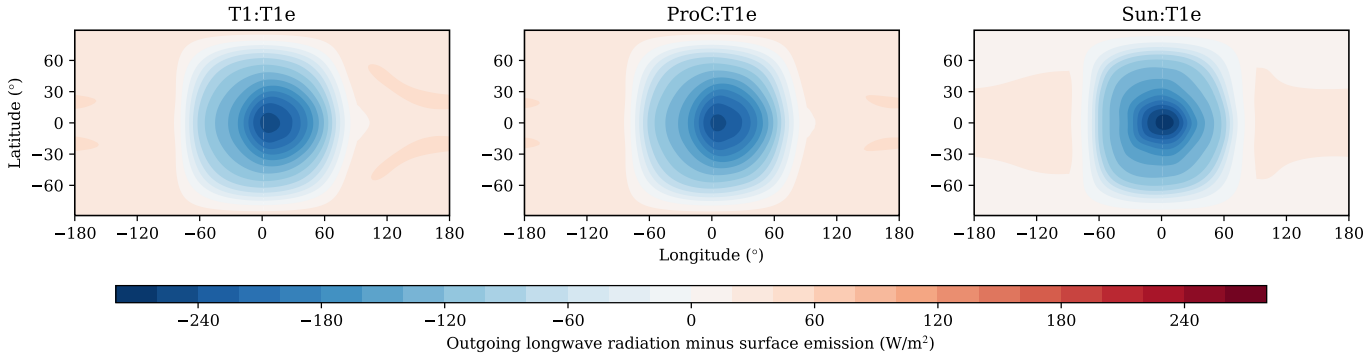

Fig. 4. Map of the OLR minus the planetary surface emission as a colour scale for simulations T1:T1e (*left*), ProC:T1e (*middle*) and Sun:T1e (*right*). A positive difference (red) indicates an increase in OLR emission relative to the surface. The sub-stellar point is located at (0°, 0°).

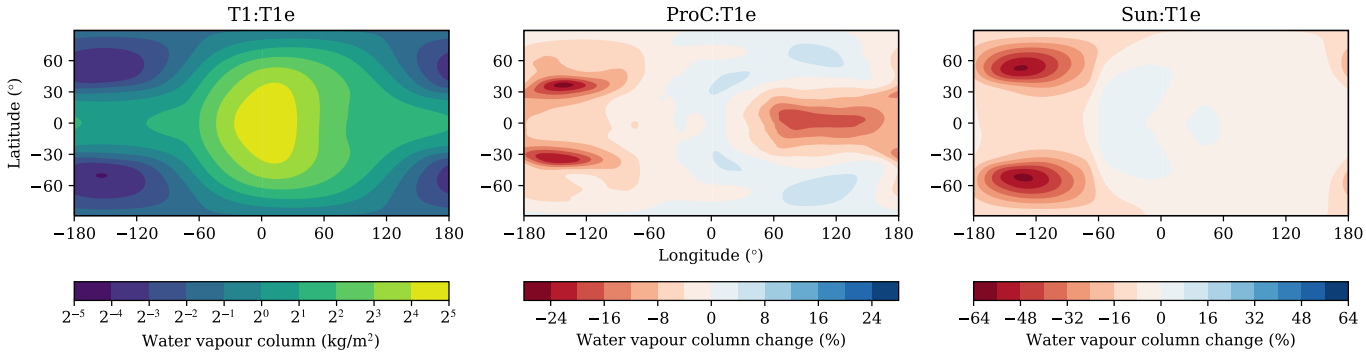

Fig. 5. Map of the column-integrated water vapour (mass of water per cross-section area, colour scale) for the T1:T1e simulation (*left*). The following two plots show the change in water-vapour column content for ProC:T1e (*middle*) and Sun:T1e (*right*) with the equivalent water-vapour column content of T1:T1e if it were at the same temperature profile as ProC:T1e and Sun:T1e, respectively, at the same relative humidity as T1:T1e. The percentage is calculated from the total water-vapour content of the column. A positive difference (blue) indicates a moister column than the T1:T1e, removing the effect of temperature on moisture from the Clausius-Clapeyron relation. The sub-stellar point is located at (0°, 0°). The scale for ProC:T1e and Sun:T1e is different.

equivalent water column content as a percentage change from cases ProC:T1e and Sun:T1e, respectively. Figure 5 shows that as the host star temperature increases (left to right), the nightside of the planets becomes relatively drier, beyond the drying through the Clausius-Clapeyron relation. This means that there is a general decrease in the relative humidity of the atmospheric column, suggesting a decrease in the atmospheric transport observed in the zonal jets in Fig. 3.

The advection of heat, moisture, and cloud from the dayside results in a nightside temperature inversion (Joshi et al. 2020), leading to the radiator fin effect discussed in Yang & Abbot (2014). The magnitude of this effect depends on the opacity on the nightside, which is determined by the water vapour and cloud content. From Fig. 5, we expect that the planets orbiting cooler stars have a stronger water-vapour greenhouse effect on the dayside, but increase the effect of the nightside radiator fin by increasing cloud content and, hence, the OLR. This can be explored further by using vertical profiles of the temperature, moisture content, and cloud fraction from our simulations. Figure 6 shows the hemispherically averaged variation with σ of air temperature (top left), specific humidity (top right), relative humidity (bottom left), and area cloud fraction (bottom right). The area cloud fraction is the area within a model grid box that is covered by cloud.

Firstly, Fig. 6 shows a clear temperature inversion on the nightside of all simulations (top left), linked to the circulation in the free atmosphere and radiative cooling of the surface. Additionally, the day-night temperature difference between the vertical profiles (top left) is also smaller for cases with cooler stars below the inversion, which is consistent with the efficiency of the day-night redistribution, which also increases toward cooler host stars.

On the dayside, with the majority of the atmosphere cooler than the surface (top left of Fig. 6), greenhouse gases and clouds decrease the OLR relative to surface emission (shown in Fig. 4). The hemispherically averaged specific humidity is highest at all levels on the dayside and nightside for case T1:T1e and lowest for case Sun:T1e (top right of Fig. 6). We would therefore expect a stronger greenhouse effect for simulation T1:T1e. For all simulations, the combination of the temperature inversion, warmer air temperatures, and stronger zonal transport leads to an increased water vapour and a higher OLR relative to the surface on the nightside. T1:T1e is the moistest of our simulations, resulting in the largest increase in OLR due to greenhouse gases, closely followed by ProC:T1e.

The relative humidity (bottom left panel of Fig. 6) shows an increase at high altitudes, which is both larger in magnitude and higher in the atmosphere for simulations T1:T1e and ProC:T1e than for case Sun:T1e. This effect has previously been noted by Yang et al. (2019a), who demonstrated that the increased high-altitude relative humidity for planets absorbing more shortwave radiation in the atmosphere resulted in an increased water-vapour greenhouse effect and therefore in a reduction in OLR. Table 4 shows the TOA radiative effects of water vapour and clouds for all our simulations. The radiative effects of water vapour and clouds were isolated through additional diagnostic radiative

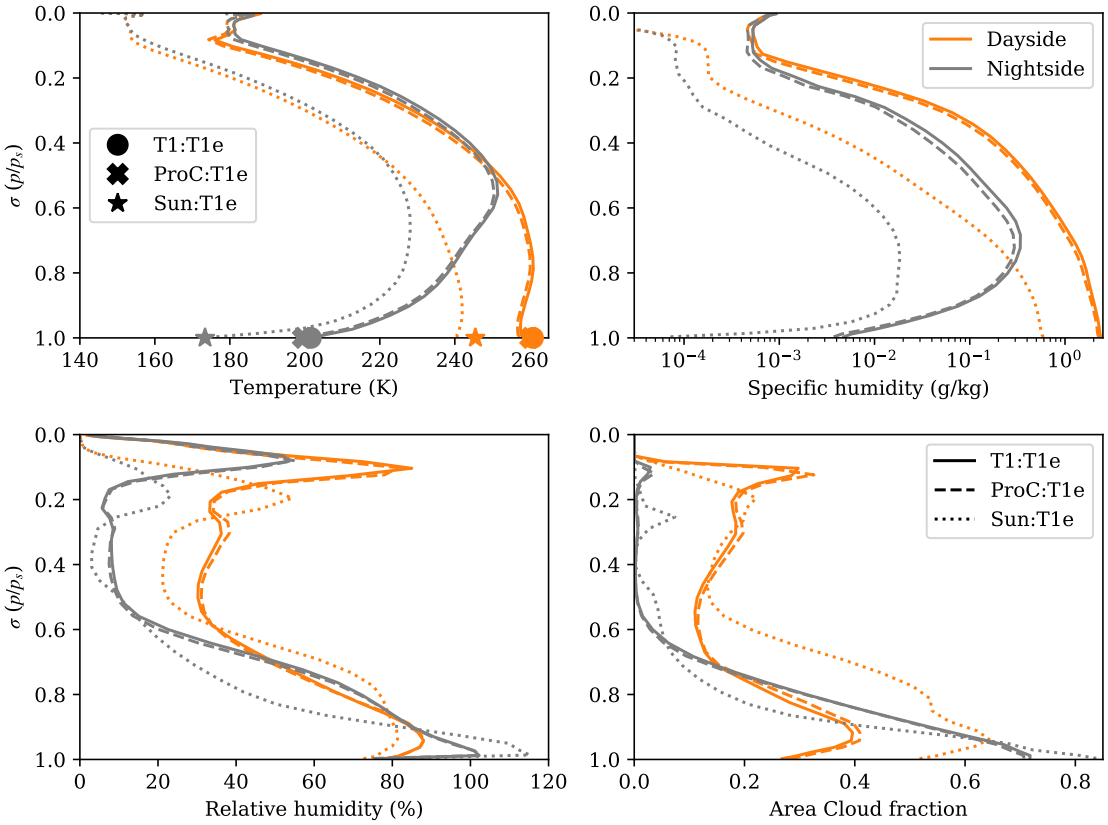

Fig. 6. Temperature (*top left*), specific humidity (*top right*), relative humidity (*bottom left*), and area cloud fraction (*bottom right*) horizontally averaged over the dayside (orange) and nightside (grey) hemispheres, plotted against σ (pressure divided by surface pressure). These are shown for all three simulations: T1:T1e (solid line), ProC:T1e (dashed line), and Sun:T1e (dotted line). The *top left panel* also includes the hemisphere-averaged surface temperatures from Table 3 as a filled circle for T1:T1e, a filled cross for ProC:T1e, and a filled star for Sun:T1e.

Table 4. Hemisphere-averaged TOA radiative effect in the shortwave (dayside only) and longwave (dayside and nightside) for both water vapour (top rows) and cloud (bottom rows), including the net value (sum of three separate terms divided by two) for simulations T1:T1e, ProC:T1e, and Sun:T1e.

Simulation	TOA radiative effect (W m^{-2})			
	Shortwave	Longwave		Net
	Dayside	Dayside	Nightside	
		Water vapour		
T1:T1e	+28.7	+9.47 (5.06%)	−21.4 (16.5%)	+8.37
ProC:T1e	+29.1	+8.65 (4.71%)	−21.5 (17.2%)	+8.14
Sun:T1e	+5.39	+0.412 (0.312%)	−15.2 (20.9%)	−4.71
		Cloud		
T1:T1e	−110	+27.0 (14.4%)	−4.58 (3.53%)	−43.8
ProC:T1e	−117	+28.2 (15.3%)	−4.07 (3.25%)	−46.4
Sun:T1e	−189	+40.7 (30.8%)	−0.822 (1.13%)	−74.5

Notes. A positive radiative effect indicates a decrease in outgoing radiation. Parentheses on the longwave TOA radiative effect include the absolute percentages of the averaged TOA outgoing longwave flux for that hemisphere. The effects of the two components are isolated using diagnostic calculations of the radiative transfer omitting their opacities (see text for explanation).

transfer calculations, which did not affect the model evolution. One calculation omitted only the water-vapour opacity, and a second calculation (called "clear-sky") omitted the radiative effects of clouds, both of which can then be compared to the baseline simulation for all cases to provide the values in Table 4. For our simulations an increased water-vapour greenhouse effect for planets orbiting cooler stars is also found (as in Yang et al. 2019a), shown in Col. 3 in the top rows of Table 4, but a clear and commensurate change in the OLR is absent from Fig. 4 because the cloud coverage contributes more to the dayside greenhouse effect, which is shown in Col. 3 in the bottom rows of the same table.

Figure 6 also shows that the dayside-averaged cloud coverage (bottom right) is largest for the warmer star, with Sun:T1e

Table 5. Dayside shortwave radiation budget hemispherically averaged for the TOA albedo and the dayside shortwave radiation absorption (as a fraction of the total TOA incoming shortwave radiation) for the T1:T1e, ProC:T1e and Sun:T1e simulations.

Simulation	Dayside TOA albedo (%)			Dayside shortwave absorption (%)			
	Total	Atmosphere	Surface	Atmosphere	Cloud	Water vapour	Surface
T1:T1e	28.8	28.0	0.767	43.0	12.2	15.6	28.3
ProC:T1e	30.6	29.8	0.790	41.1	11.0	15.3	28.3
Sun:T1e	54.8	53.6	1.24	11.5	4.38	2.78	33.7

Notes. The dayside albedo has been decomposed into an atmospheric and a surface contribution following Donohoe & Battisti (2011). The dayside shortwave radiation absorption is shown for the atmosphere and surface, with the former decomposed into cloud and water-vapour contribution by comparing the baseline model to the calculations where these radiative effects have been omitted (see text for explanation).

Table 6. Hemisphere-averaged OLR budget for the dayside and nightside as a percentage of the non-reflected shortwave radiation absorbed by the planet, shown for simulations T1:T1e, ProC:T1e, and Sun:T1e.

Simulation	OLR budget (%)	
	Dayside	Nightside
T1:T1e	59.1	40.9
ProC:T1e	59.5	40.5
Sun:T1e	64.5	35.5

having a ~60% larger peak than T1:T1e and ProC:T1e, at around $\sigma = 0.9$. Cloud coverage on the dayside can cool the planet by increasing the TOA albedo. This is demonstrated in Table 5, which shows the dayside albedo and total shortwave absorption as fractions of the total TOA incident stellar flux, in particular the second column.

The total albedo increases for hotter stars, see Cols. 2–4 in Table 5, partially because the surface albedo increases, but this is predominantly caused by increased cloud coverage, as shown in Col. 2 in the bottom rows of Table 4. Table 5 shows that the albedo is highest for simulation Sun:T1e and lowest for case T1:T1e, which has the lowest dayside cloud coverage (clouds are equally reflective in each case, see Fig. 1). This is the dominant cause for the decrease in surface temperatures in Fig. 2 and air temperatures; case Sun:T1e is ~15-20 K cooler for all σ on the dayside in Fig. 6 (top left grey). Cloud also affects the OLR budget, which is shown in Cols. 3 and 4 in the bottom rows of Table 4, which show the cloud radiative effect. On the dayside, cloud increases the longwave radiation retained by the atmosphere, which decreases the OLR. However, this effect is about four times smaller than the shortwave cloud radiative effect, which is the dominant factor in the overall decrease in planetary temperature for hotter stars.

On the nightside, the OLR is increased through cloud radiative effects. Near the surface, there is more cloud for simulation Sun:T1e than in the two other cases (Fig. 6, bottom right). Near-surface cloud has a weaker effect on the cloud radiative effect as the cloud temperature is more similar to that of the surface than are the remaining temperatures below the inversion maxima. Because of the nightside temperature inversion, the atmosphere at $\sigma > 0.2$ for all simulations is warmer than the planetary surface and thus radiates heat into space more efficiently, which increases the cloud radiative effect and cools the planet. Cases T1:T1e and ProC:T1e both have more cloud between $0.6 < \sigma < 0.9$ than case Sun:T1e, which leads to an increase in the nightside OLR relative to the clear-sky case, shown in Col. 4 in the bottom rows of Table 4. The radiator fin effect is stronger for planets with more efficient day-night circulation because the nightside cloud and water vapour content is higher. Table 6 shows the TOA outgoing radiation budget as the dayside and nightside OLR as a percentage of the non–reflected shortwave radiation. Table 6 demonstrates an increase in the proportion of total radiation emitted by the planet coming from the nightside for cooler stars. This might suggest that planets orbiting cooler stars, which we have shown have generally a more efficient circulation, are cooler overall. However, our simulations show the reverse, where the cooler host star results in an overall warmer planetary climate, showing that the changes in dayside cloud albedo are the dominant mechanism (Yang et al. 2013). This is clearly shown in the bottom rows of Table 4, where the shortwave dayside cloud radiative effect is strongest and dominates the net cloud radiative effect, which also increases with host star temperature, leading to the strongest planetary cooling.

Table 5 shows that the shortwave reflection (albedo) on the dayside is highest for simulation Sun:T1e and lowest for the T1:T1e. The method described by Donohoe & Battisti (2011) was used to determine the atmospheric and surface contributions to the TOA dayside albedo, with the atmosphere as the dominant contribution at ~97.5% for all simulations. The surface contribution has been significantly attenuated by the atmosphere, reducing the surface albedo by ~90% of the actual value for all the simulations. The majority of this atmospheric albedo is produced through cloud scattering, which is the dominant contribution to the TOA shortwave cloud radiative effect compared to cloud absorption (Col. 2 in the bottom rows of Table 4). The remaining outgoing radiation budget, emitted as longwave radiation, may be distributed between dayside and nightside emission and is shown in Table 6. The proportion of the remaining radiation increases in favour of emission on the dayside for planets orbiting hotter stars, as demonstrated by the increased day-night surface temperature contrast, as shown in Table 3. This occurs even with an increase in cloud that suppresses longwave emission on the dayside (Col. 3 in the bottom rows of Table 4). The water-vapour greenhouse effect has the opposite effect: it decreases in hotter stars (Col. 3 in the top rows of Table 4), but its effect is weaker than that of the cloud.

On the nightside, both cloud and water vapour increase the nightside OLR emission due to the temperature inversion (Col. 4 in Table 4), which enhances the radiator fin effect. For water vapour, this effect in terms of the total radiation budget decreases for cooler stars, but when it is compared to the total nightside OLR (parentheses), it increases with host star temperature. For the cloud, this decreases for both interpretations, and their combined effects contribute ~20% of the nightside OLR. The nightside radiator fin effect is thus dominated by the day-night temperature contrast of the surface, rather than the overall cloud

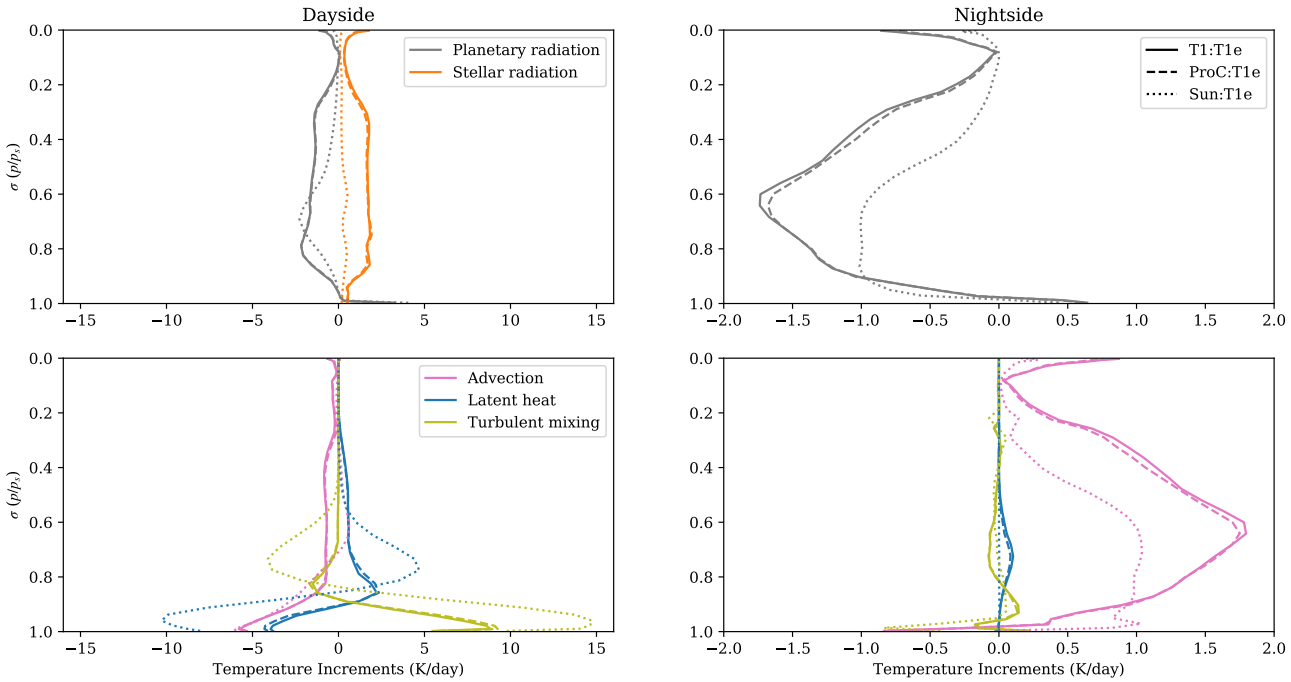

Fig. 7. Rate of change of temperature or heating profiles, known as temperature increments, plotted against σ (pressure divided by surface pressure) for simulations T1:T1e (solid lines), ProC:T1e (dashed lines), and Sun:T1e (dotted lines) for each component process. The processes shown are atmospheric absorption of stellar radiation (orange, *top panels*), thermal emission or absorption of planetary radiation (grey, *top panels*), large-scale circulation, known as advection, (pink, *bottom panels*), latent heating or cooling of water (blue, *bottom panels*), and turbulent mixing (green, *bottom panels*). The day- and nightside hemispherically averaged values are shown in the *left* and *right panels*, respectively. The *x*-axis limits are different between the day- and nightside panels. In equilibrium the net heating is zero.

or water-vapour structure in the atmosphere, which maintains a similar contribution to the total nightside OLR.

The global net TOA water-vapour radiative effect (Col. 5 in Table 4) is an order of magnitude smaller than the net cloud radiative effect and changes sign between the M dwarf and G dwarf orbiting simulations. Table 4 shows that in T1:T1e and ProC:T1e, water vapour has a net warming effect on the global budget, while in case Sun:T1e, water vapour has a net cooling effect. The difference is mainly attributed to the decrease in shortwave absorption (Col. 2 in Table 4) for hotter stars, but also to the decrease in water-vapour greenhouse effect stemming from the decrease in moisture in the upper atmosphere on the dayside (Fig. 6).

3.3. Heat and moisture budgets

To further isolate the key or dominant processes, we separated the various contributions to the atmospheric temperature and specific humidity changes. Figure 7 shows the hemisphere-averaged heating rates, or temperature increments, as a function of σ for the dayside (left panels) and nightside (right panels). For the dayside radiation (top left panel, Fig. 7), direct stellar radiation heats the atmosphere in cases T1:T1e and ProC:T1e, predominantly for $0.2 < \sigma < 0.9$, at ~2 K day^{-1}, and the stellar heating of the atmosphere is significantly reduced in case Sun:T1e. For simulations T1:T1e and ProC:T1e, the region where $\sigma < 0.7$ is close to radiative equilibrium (planetary radiation balances stellar radiation), which is not the case for Sun:T1e until much higher in the atmosphere, $\sigma \lesssim 0.3$. The atmospheric absorption of stellar radiation is further quantified in Table 5, which shows the dayside atmospheric absorption as a percentage of the incident TOA shortwave radiation. This is nearly four times higher for case T1:T1e than in case Sun:T1e; the T1:T1e atmosphere absorbs 1.9% more stellar radiation than case ProC:T1e.

The direct heating of the middle to upper troposphere by cooler stars leads to an increase in convective stability in cases T1:T1e and ProC:T1e, reducing the vertical transport of moisture and thus the height and magnitude of the latent heating term on the dayside (bottom left panel, Fig. 7). This is supported by the dayside cloud coverage shown in Fig. 6, with case Sun:T1e exhibiting more cloud at $\sigma > 0.5$ than cases T1:T1e and ProC:T1e. As a result of a reduced atmospheric absorption of non-reflected shortwave radiation, case Sun:T1e experiences an increased proportion of (non-reflected) stellar radiation absorbed at the surface on the dayside (Table 5, compare Cols. 5 and 8), than the simulations with cooler host stars. This leads to higher turbulent flux heating in the boundary layer, which is balanced by latent cooling from evaporation of precipitation from increased cloud and advective cooling (bottom left panel, Fig. 7). The shortwave atmospheric absorption is isolated for both cloud and water vapour in Table 5 (Cols. 6 and 7, respectively). Although the effects of both are of a similar order of magnitude for each simulation, for planets orbiting M dwarfs, water vapour contributes more to atmospheric absorption than clouds, while the opposite is true for G dwarfs. The remaining contribution to shortwave atmospheric absorption is carbon dioxide, which is held at a constant concentration in our simulations.

On the nightside (right panels, Fig. 7), advective heating is balanced by cooling through planetary radiation emission. Advective heating comes from transport of heat from the dayside, producing the temperature inversions seen in Fig. 6, and is highest for case T1:T1e, which follows from the stronger equatorial jets seen for planets orbiting cooler stars (Fig. 3). The relatively dry atmosphere on the nightside and the lack of stellar

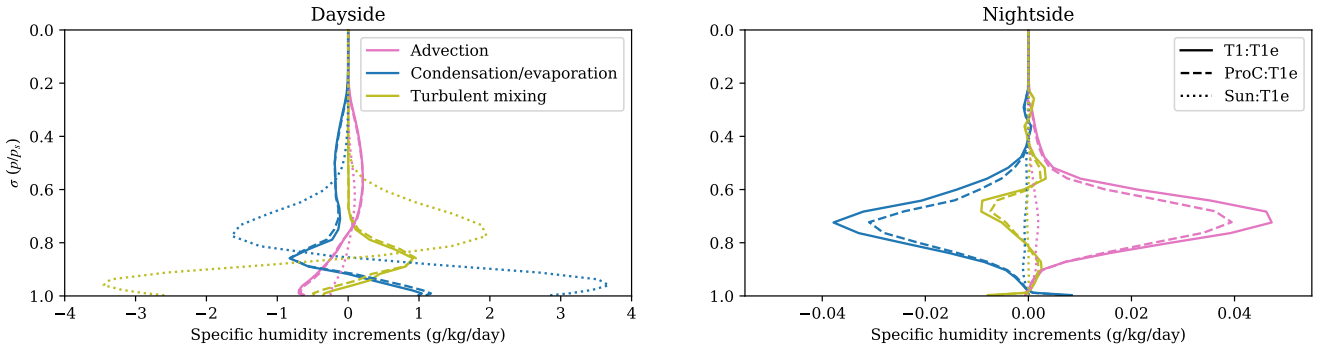

Fig. 8. Rate of change of the specific humidity, known as specific humidity increments, plotted against σ (pressure divided by surface pressure) for simulations T1:T1e (solid lines), ProC:T1e (dashed lines), and Sun:T1e (dotted lines) for each component process. The processes shown are the large-scale circulation, known as advection, (pink), condensation or evaporation (blue), and turbulent mixing (green). The day- and nightside hemispherically averaged values are shown in the *left* and *right panels*, respectively. The x-axis limits are different between the day- and nightside panels. In equilibrium the net heating is zero.

heating at the surface result in low latent heating and boundary layer contributions (bottom right panel, Fig. 7).

Similarly to the temperature increments, we isolated the contributions from different physical processes to the moisture budget in our simulations. Figure 8 shows the rate of change of specific humidity in a similar format as in Fig. 7. On the dayside (left, Fig. 8), turbulent mixing transports water vapour from near the surface to the mid-troposphere ($0.5 < \sigma < 0.85$), where it condenses, precipitates, and then evaporates again in the boundary layer ($\sigma > 0.85$). The large-scale transport is strongest for the T1:T1e case, which is shown in the specific humidity increment due to advection. Cool dry air is advected, returning from the nightside near the surface, and moist warm air is transported vertically, reducing moisture near the surface. Simulation T1:T1e has the highest nightside advection of water vapour (right, Fig. 8), and the lowest is found in case Sun:T1e. On the dayside, advection reduces specific humidity near the surface. The minima for the specific humidity increment due to advection are largest for cases T1:T1e and ProC:T1e, which may be due to a stronger return flow from the nightside. Evaporation, condensation and boundary layer effects occur deeper in the atmosphere for case Sun:T1e than in the remaining simulations, suggesting that convection becomes deeper for hotter host stars. On the nightside (right, Fig. 8), moist air is transported in by advection from the dayside, where it condenses to form nightside cloud. The cloud forms mainly around $\sigma = 0.7$, where it descends to near the surface, as shown in Fig. 6, where the cloud area fraction is highest there.

Our results have isolated the effect that different host star spectra have on the simulated planetary climate of a tidally locked terrestrial exoplanet, with a modern-day Earth-like atmosphere. With all else held constant, a planet orbiting a cooler star such as TRAPPIST-1 or Proxima Centauri absorbs more radiation directly in the atmosphere than a planet orbiting the Sun, similar to the results of Shields et al. (2013) for rapidly rotating non-tidally locked planets. Increased atmospheric stellar radiation absorption leads to a decrease in the proportion of radiation that is absorbed by the planetary surface and to an increase in static stability and a decrease in convection, leading to reduced dayside cloud coverage. This decreases the albedo and leads to a warmer planet: simulation T1:T1e is globally 1.4 and 21.8 K warmer than cases ProC:T1e and Sun:T1e, respectively. The day-night temperature and atmospheric moisture content contrast is also lowest for case T1:T1e.

4. Conclusions

We have used the Met Office 3D GCM to compare simulations of the climates of a planet orbiting three different host stars, two of which are M dwarfs known to be orbited by near Earth-sized planets in their habitable zone. The third planet was the Sun, a G dwarf. We assumed an Earth-like atmospheric composition and a tidally locked state. With stellar irradiance and other planetary parameters held constant, planets orbiting cooler stars experience an increased proportion of incident radiation that is absorbed directly by the troposphere compared to the surface. This is due to the increase in the ability of cloud, water vapour, and carbon dioxide to absorb stellar radiation when cooler stars are orbited. This leads to an atmosphere that is more statically stable, reducing dayside convection and thus cloud coverage compared to hotter stars. For these planets orbiting hotter stars, increasing cloud coverage increases the planetary albedo, which decreases the overall proportion of radiation absorbed by the planet, but maintains a lower ratio of atmospheric to planetary surface absorption. The reduction in albedo causes planets orbiting cooler stars to be globally warmer, and atmospheric transport of heat and moisture from the dayside to the nightside is more efficient because the equatorial jets are stronger. This decreases the ratio of dayside to nightside OLR. We find that the combined contribution of water vapour and cloud to the nightside radiator fin effect is enhanced to a similar degree for all stellar types, contributing ~20% of the nightside OLR for M and G dwarfs. Overall, of planets near the outer edge of the habitable zone that have an Earth-like composition, those orbiting cooler stars may be considered more habitable than similar counterparts orbiting hotter stars because they are likely to have a larger surface region that can support liquid water.

It is important to note that all our simulations adopted the current planetary parameters estimated for TRAPPIST-1e, and the stellar spectrum was varied. The total stellar irradiance was held constant by varying the orbital semi-major axis only between simulations, but a tidally locked configuration was retained. Therefore the two additional simulations irradiated by Proxima Centauri and the Sun were not designed to represent any real planet, and the resulting rotation rate was inconsistent with the orbital period and tidally locked state (as the rotation period should increase with semi-major axis for a tidally locked planet). We have designed our simulations such as to isolate the impacts of a different host star spectrum on the simulated planetary climates.

Our method, however, has important limitations that must be addressed with additional research that is beyond the scope of this study. As M dwarfs are more active than G dwarfs, and the planet must orbit closer to the host star to intercept similar stellar flux levels, the impact of flares and high-energy radiation must be considered (e.g. see Tilley et al. 2019). Concerted studies in 3D are required to explore the interaction of the stellar activity with the atmosphere, and in particular, the potential impacts on the O_3 distribution, given that tidal locking gives rise to a permanent day- and nightside, the latter never receiving direct stellar radiation. This work has begun for quiescent host stars (Yates et al. 2020), and we are working on extending it to include host star activity. Furthermore, the atmospheric composition in our simulations was kept constant in a simplified Earth-like configuration. It is clear from our own Solar System that terrestrial planets can have extremely different compositions. In this study we focused on the impacts of stellar spectra on climate and potential implications on habitability, therefore we based our work on the only currently known inhabited planet, Earth. However, Earth has sustained life through very different atmospheric compositions, given the first evidence of life on Earth is from at least as early as 3.7 Ga (Rosing 1999; Hassenkam et al. 2017).

Potentially important climate processes or mechanisms have also been omitted, such as atmospheric chemistry (e.g. ozone in Yates et al. 2020), land-surface impact (e.g. Lewis et al. 2018), dust (e.g. Boutle et al. 2020), ocean heat transport (e.g. Yang & Abbot 2014; Yang et al. 2019b; Del Genio et al. 2019), and perhaps sea- or land-ice (Rose et al. 2017). In particular, Yang & Abbot (2014) and Del Genio et al. (2019) found that ocean transport also acts to reduce the day-night temperature contrast. Inclusion of ocean heat transport would be expected to decrease our predicted day-night temperature contrasts and dayside convection. However, the ocean transport is sensitive to the configuration of land and ocean (Yang et al. 2019b). Additionally, ice formation may lead to a cooling of all our simulations if it were included, and it might increase the differences between the M dwarf cases and the simulation using the Sun because the ice albedo under G dwarf stellar spectra is higher (Shields et al. 2013). However, as ice formation might well be limited to the nightside, its effect on the overall climate of a tidally locked planet could be weak. The reduction in ice albedo from hotter to cooler host stars suggests that their orbiting planets may be more resistant to entering a "snowball" state (Rushby et al. 2019), which has occurred at least three times for Earth (e.g. Lenton & Watson 2011). Several studies have questioned whether the climate of tidally locked planets can exist in a stable regime and avoid atmospheric collapse (Kasting et al. 2014; Turbet et al. 2018). The reduced day-night temperature contrast found in our simulations irradiated by cooler host stars may aid their atmospheric stability.

The adoption of a fixed Earth-like atmospheric composition also neglects the impact of the stellar irradiation on the long-term evolution of the atmosphere, which is required to determine the likely atmospheric composition. However, this is a difficult and poorly constrained problem (Bolmont et al. 2017; Dong et al. 2018). Finally, we did not consider the impact of life itself. The presence of life on terrestrial exoplanets may fundamentally alter the atmospheric composition (Nicholson et al. 2018; Vecchio et al. 2020), as has likely happened throughout Earth's own history (Lenton & Watson 2011; Lenton et al. 2018). We must also consider that photosynthesis on Earth is highly adapted towards the spectra it receives and the consequences this may have on the evolution of life (Lingam & Loeb 2019; Lingam & Loeb 2020).

Acknowledgements. We are grateful to Professor Jun Yang, whose comments during the review process significantly improved this manuscript. JE would like to thank the Hill Family Scholarship. The Hill Family Scholarship has been generously supported by University of Exeter alumnus, and president of the University's US Foundation Graham Hill (Economic & Political Development, 1992) and other donors to the US Foundation. Material produced using Met Office Software. NM and TL gratefully acknowledge funding from a Leverhulme Trust Research Project Grant. J.M. and I.B. acknowledge the support of a Met Office Academic Partnership secondment. We acknowledge use of the Monsoon system, a collaborative facility supplied under the Joint Weather and Climate Research Programme, a strategic partnership between the Met Office and the Natural Environment Research Council. This research made use of the ISCA High Performance Computing Service at the University of Exeter. This work was performed using the DiRAC Data Intensive service at Leicester, operated by the University of Leicester IT Services, which forms part of the STFC DiRAC HPC Facility (www.dirac.ac.uk). The equipment was funded by BEIS capital funding via STFC capital grants ST/K000373/1 and ST/R002363/1 and STFC DiRAC Operations grant ST/R001014/1. DiRAC is part of the National e-Infrastructure. This work was partly supported by a Science and Technology Facilities Council Consolidated Grant (ST/R000395/1). We would like to thank David Admundsen and NASA GISS for the use of their spectral files in these simulations. The research data supporting this publication are openly available from the University of Exeter's institutional repository at: https://doi.org/10.24378/exe.2383

References

Amundsen, D. S., Baraffe, I., Tremblin, P., et al. 2014, A&A, 564, A59
Amundsen, D. S., Mayne, N. J., Baraffe, I., et al. 2016, A&A, 595, A36
Amundsen, D. S., Tremblin, P., Manners, J., Baraffe, I., & Mayne, N. J. 2017, A&A, 598, A97
Anglada-Escudé, G., Amado, P. J., Barnes, J., et al. 2016, Nature, 536, 437
Bolmont, E., Selsis, F., Owen, J. E., et al. 2017, MNRAS, 464, 3728
Boutle, I. A., Mayne, N. J., Drummond, B., et al. 2017, A&A, 601, A120
Boutle, I. A., Joshi, M., Lambert, F. H., et al. 2020, Nat. Commun., 11, 2731
Brown, A. R., Beare, R. J., Edwards, J. M., et al. 2008, Boundary-Layer Meteorol., 128, 117
Debras, F., Mayne, N., Baraffe, I., Goffrey, T., & Thuburn, J. 2019, A&A, 631, A36
Debras, F., Mayne, N., Baraffe, I., et al. 2020, A&A, 633, A2
Del Genio, A. D., Way, M. J., Amundsen, D. S., et al. 2019, Astrobiology, 19, 99
Dong, C., Jin, M., Lingam, M., et al. 2018, Proc. Natl. Acad. Sci., 115, 260
Donohoe, A., & Battisti, D. S. 2011, J. Clim., 24, 4402
Drummond, B., Mayne, N. J., Manners, J., et al. 2018a, ApJ, 855, L31
Drummond, B., Mayne, N. J., Manners, J., et al. 2018b, ApJ, 869, 28
Drummond, B., Mayne, N. J., Baraffe, I., et al. 2018c, A&A, 612, A105
Drummond, B., Hébrard, E, Mayne, N. J., et al. 2020, A&A, 636, A68
Fauchez, T., Turbet, M., Wolf, E. T., et al. 2020, Geosci. Model Dev., 13, 707
Frierson, D. M. W., Held, I. M., & Zurita-Gotor, P. 2006, J. Atm. Sci., 63, 2548
Gillon, M., Triaud, A. H. M. J., Demory, B., et al. 2017, Nature, 542, 456
Gregory, D., & Rowntree, P. R. 1990, Mon. Weather Rev., 118, 1483
Grimm, S. L., Demory, B., Gillon, M., et al. 2018, A&A, 613, A68
Haqq-Misra, J., Wolf, E. T., Joshi, M., Zhang, X., & Kopparapu, R. K. 2018, ApJ, 852, 67
Hassenkam, T., Andersson, M. P., Dalby, K. N., Mackenzie, D. M. A., & Rosing, M. T. 2017, Nature, 548, 78
Helling, C., Lee, G., Dobbs-Dixon, I., et al. 2016, MNRAS, 460, 855
Howard, W. S., Tilley, M. A., Corbett, H., et al. 2018, ApJ, 860, L30
Hunter, J. D. 2007, Compu.Sci. Eng., 9, 90
Jin, Z., Qiao, Y., Wang, Y., Fang, Y., & Yi, W. 2011, Opt. Express, 19, 26429
Joshi, M. M., & Haberle, R. M. 2012, Astrobiology, 12, 3
Joshi, M. M., Elvidge, A. D., Wordsworth, R., & Sergeev, D. 2020, ApJ, 892, L33
Kasting, J. F., Whitmire, D. P., & Reynolds, R. T. 1993, Icarus, 101, 108
Kasting, J. F., Kopparapu, R., Ramirez, R. M., & Harman, C. E. 2014, Proc. Natl. Acad. Sci., 111, 12641
Koll, D. D. B., & Abbot, D. S. 2016, ApJ, 825, 99
Komacek, T. D., & Abbot, D. S. 2019, ApJ, 871, 245
Lenton, T. M., & Watson, A. J. 2011, Revolutions that Made the Earth (Oxford: Oxford University Press)

Lenton, T. M., Daines, S. J., & Mills, B. J. 2018, Earth-Science Reviews, 178, 1
Lewis, N. T., Lambert, F. H., Boutle, I. A., et al. 2018, ApJ, 854, 171
Lines, S., Mayne, N. J., Boutle, I. A., et al. 2018a, A&A, 615, A97
Lines, S., Manners, J., Mayne, N. J., et al. 2018b, MNRAS, 481, 194
Lines, S., Mayne, N. J., Manners, J., et al. 2019, MNRAS, 488, 1332
Lingam, M., & Loeb, A. 2019, MNRAS, 485, 5924
Lingam, M., & Loeb, A. 2020, ApJ, 889, L15
Lock, A. P., Brown, A. R., Bush, M. R., Martin, G. M., & Smith, R. N. B. 2000, Mon. Weather Rev., 128, 3187
Mayne, N. J., Baraffe, I., Acreman, D. M., et al. 2014a, A&A, 561, A1
Mayne, N. J., Baraffe, I., Acreman, D. M., et al. 2014b, Geosci. Model Dev., 7, 3059
Mayne, N. J., Debras, F., Baraffe, I., et al. 2017, A&A, 604, A79
Mayne, N. J., Drummond, B., Debras, F., et al. 2019, ApJ, 871, 56
Merlis, T. M., & Schneider, T. 2010, J. Adv. Modeling Earth Sys., 2, 4
Met Office 2010-2020, Iris: A Python library for analysing and visualising meteorological and oceanographic data sets
Nicholson, A. E., Wilkinson, D. M., Hywel T P Williams, H. T. P., & Lenton, T. M. 2018, MNRAS, 477, 727
Penn, J., & Vallis, G. K. 2018, ApJ, 868, 147
Pierrehumbert, R. T. 2010, Principles of Planetary Climate (Cambridge: Cambridge University Press)
Pierrehumbert, R. T., & Hammond, M. 2019, Ann. Rev. Fluid Mech., 51, 275
Polyansky, O. L., Kyuberis, A. A., Zobov, N. F., et al. 2018, MNRAS, 480, 2597
Rajpurohit, A. S., Reylé, C., Allard, F., et al. 2013, A&A, 556, A15
Rose, B. E. J., Cronin, T. W., & Bitz, C. M. 2017, ApJ, 846, 28
Rosing, M. T. 1999, Science, 283, 674
Rushby, A. J., Shields, A. L., & Joshi, M. 2019, ApJ, 887, 29
Sainsbury-Martinez, F., Wang, P., Fromang, S., et al. 2019, A&A, 632, A114
Schlaufman, K. C., & Laughlin, G. 2010, A&A, 519, A105
Sergeev, D. E., Lambert, F. H., Mayne, N. J., et al. 2020, ApJ, 894, 84
Shields, A. L., Meadows, V. S., Bitz, C. M., et al. 2013, Astrobiology, 13, 715
Shields, A. L., Bitz, C. M., & Palubski, I. 2019, ApJ, 884, L2
Showman, A. P., & Polvani, L. M. 2010, Geophys. Res. Lett., 37, L18811
Showman, A. P., & Polvani, L. M. 2011, ApJ, 738, 71
Tashkun, S., & Perevalov, V. 2011, J. Quant. Spectr. Rad. Transf., 112, 1403
Tennyson, J., Yurchenko, S. N., Al-Refaie, A. F., et al. 2016, J. Mol. Spectr., 327, 73
Thomson, S. I., & Vallis, G. K. 2019, Q. J. R. Meteorol. Soc., 145, 2627
Tilley, M. A., Segura, A., Meadows, V., Hawley, S., & Davenport, J. 2019, Astrobiology, 19, 64
Tremblin, P., Chabrier, G., Mayne, N. J., et al. 2017, ApJ, 841, 30
Turbet, M., Leconte, J., Selsis, F., et al. 2016, A&A, 596, A112
Turbet, M., Bolmont, E., Leconte, J., et al. 2018, A&A, 612, A86
Vecchio, A., Primavera, L., Lepreti, F., Alberti, T., & Carbone, V. 2020, ApJ, 891, 24
Walters, D., Baran, A. J., Boutle, I., et al. 2019, Geosci. Model Dev., 12, 1909
Wilson, D. R., & Ballard, S. P. 1999, Q. J. R. Meteorol. Soc., 125, 1607
Wilson, D. R., Bushell, A. C., Kerr-Munslow, A. M., Price, J. D., & Morcrette, C. J. 2008, Q. J. R. Meteorol. Soc., 134, 2093
Wolf, E. T. 2017, ApJ, 839, L1
Wood, N., Staniforth, A., White, A., et al. 2014, Q. J. R. Meteorol. Soc., 140, 1505
Yang, J., & Abbot, D. S. 2014, ApJ, 784, 155
Yang, H., & Yang, J. 2019, ArXiv e-prints [arXiv:1910.06479]
Yang, J., Cowan, N. B., & Abbot, D. S. 2013, ApJ, 771, L45
Yang, J., Leconte, J., Wolf, E. T., et al. 2019a, ApJ, 875, 46
Yang, J., Abbot, D. S., Koll, D. D. B., Hu, Y., & Showman, A. P. 2019b, ApJ, 871, 29
Yates, J. S., Palmer, P. I., Manners, J., et al. 2020, MNRAS, 492, 1691
Yurchenko, S. N., Al-Refaie, A. F., & Tennyson, J. 2018, A&A, 614, A131